nature portfolio

https://doi.org/10.1038/s41561-022-00963-w

Supplementary information

Lower oceanic crust formed by in situ melt crystallization revealed by seismic layering

In the format provided by the authors and unedited

Lower oceanic crust formed by in situ melt crystallisation revealed by seismic layering

Peng Guo[1,*], Satish C. Singh[2], Venkata A. Vaddineni[2], Ingo Grevemeyer[3] and Erdinc Saygin[1,4]

1. Deep Earth Imaging Future Science Platform, The Commonwealth Scientific and Industrial Research Organisation (CSIRO), Kensington 6151, Australia; peng.guo@csiro.au

2. Laboratoire de Géosciences Marines, Institut de Physique du Globe de Paris, Université de Paris Cité, Paris 75005, France;

3. GEOMAR Helmholtz Centre for Ocean Research, D-24148 Kiel, Germany

4. Department of Physics, School of Physics, Mathematics and Computing, Faculty of Engineering and Mathematical Sciences, University of Western Australia, Crawley 6009, Australia

This file contains supplementary figures Figs. S1 – S24.

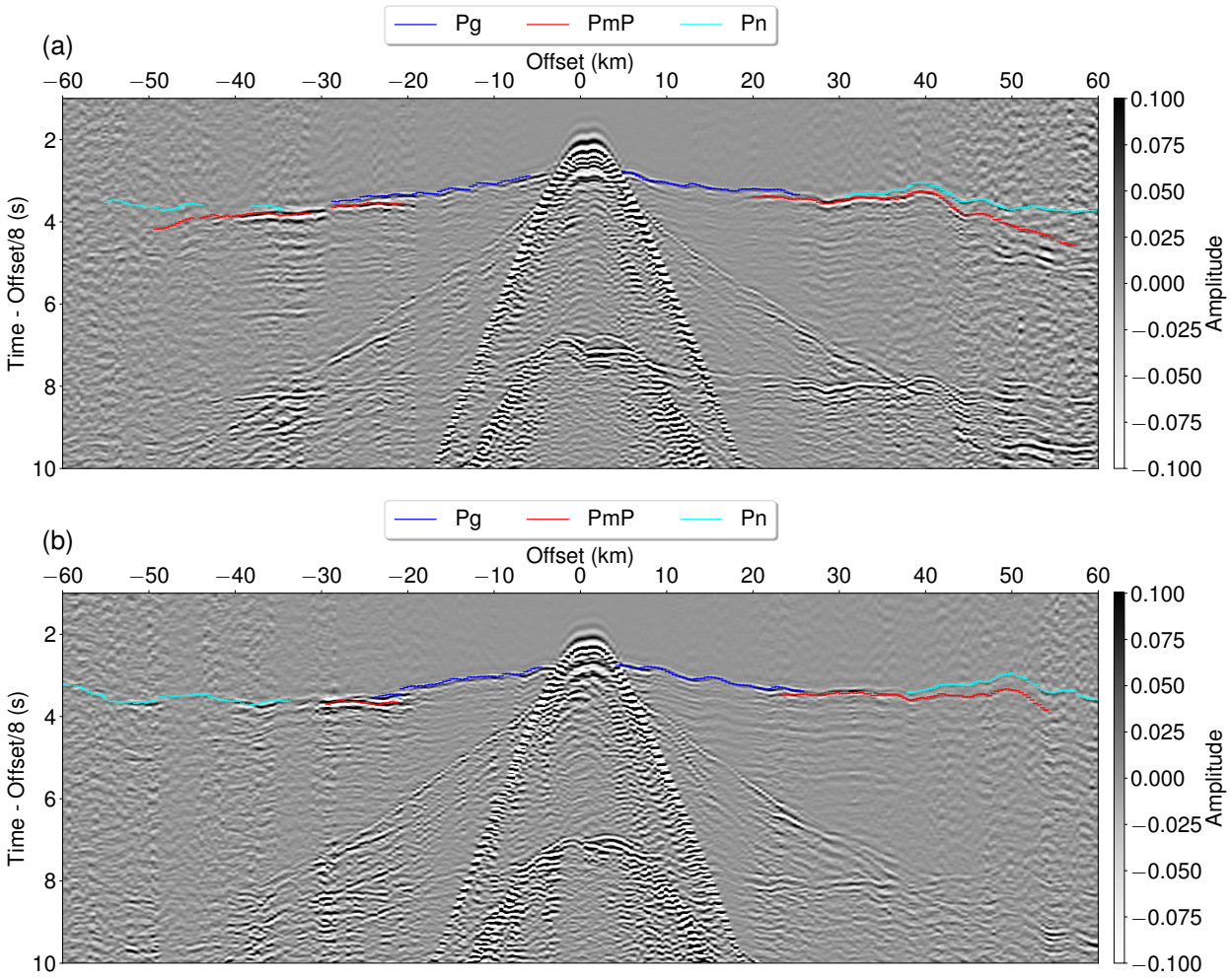

Fig. S1: The field OBS data for OBS 57 and 58 after pre-processing. The crustal turning waves (blue), the Moho reflections (red) and mantle refractions (cyan) are labelled.

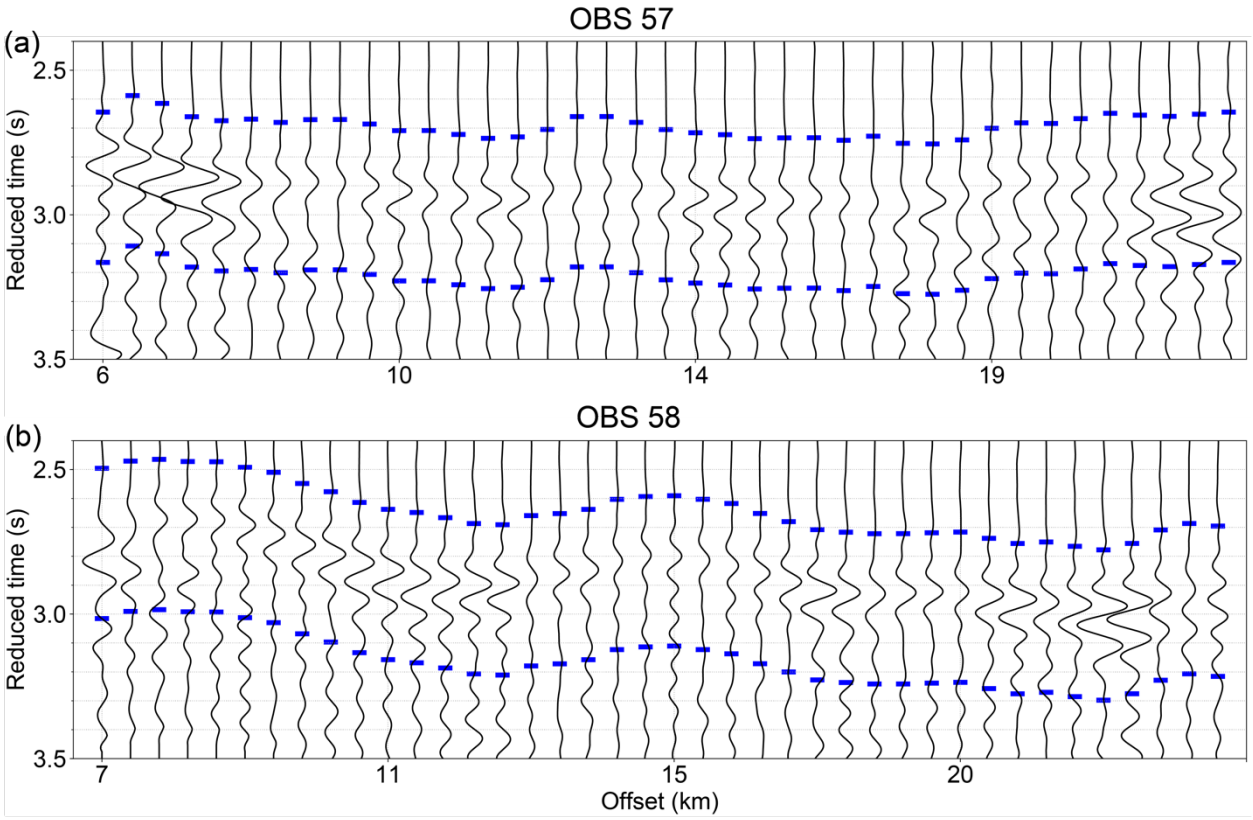

Fig. S2: Data for OBS 57 and 58. The dashed blue lines show the 0.5 s time window (0.2 s prior and 0.3s after the travel time picking) that was used for isolating the Pg arrivals for FWI. The waveforms of the first arrivals are included in the time window.

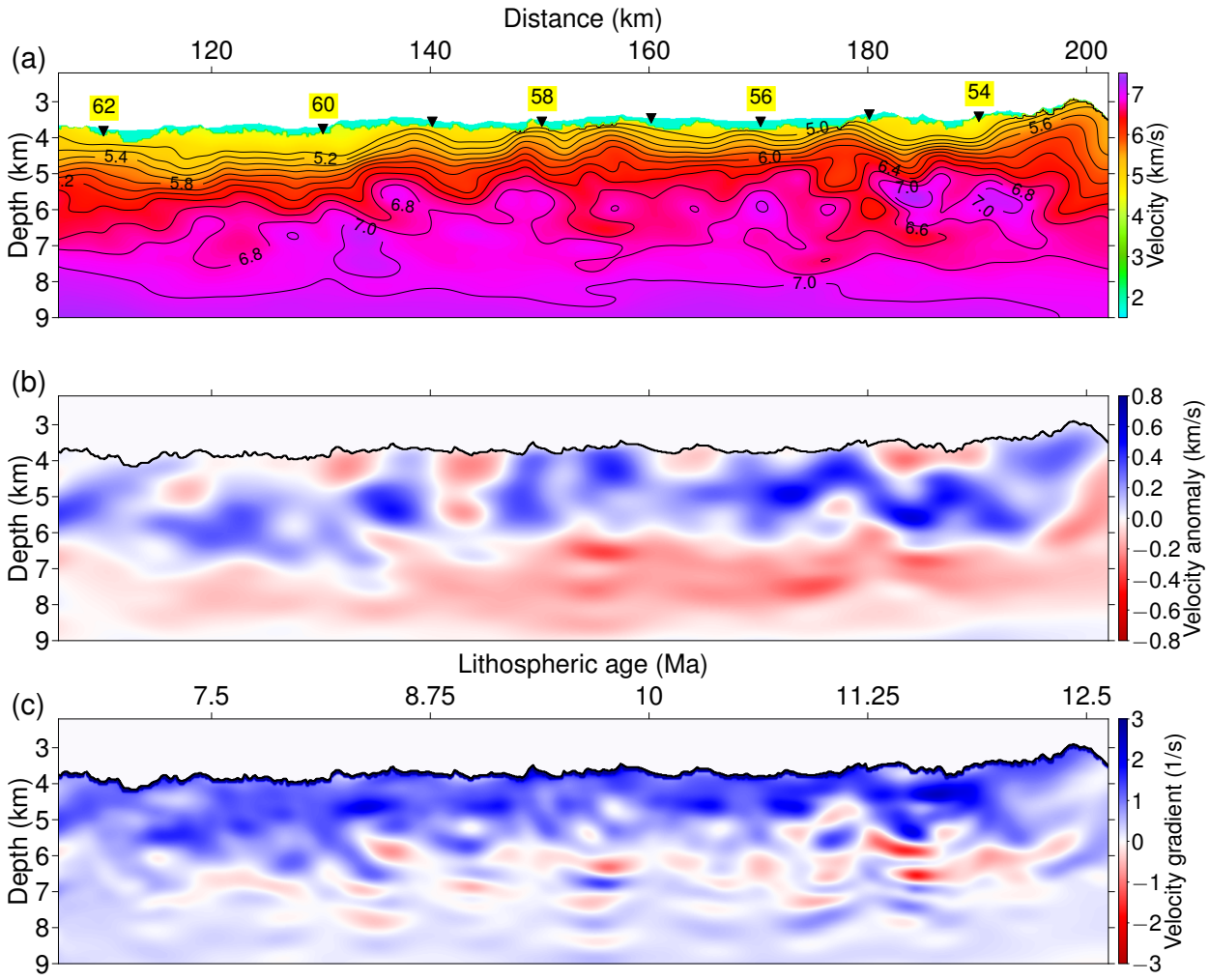

Fig. S3: Seismic velocity models of the oceanic crust from the 'true-amplitude' FWI using near-to-intermediate offsets (the first phase of the 'true-amplitude' FWI)**.** The data used for FWI is from ± 6-8 km up to ±15 km offsets. A Gaussian smoothing operator (smoothing lengths of 2 km and 0.4 km in the horizontal and vertical directions, respectively) was applied for velocity update. (a) The velocity model from the 'true-amplitude' FWI, (b) the velocity anomaly (the difference between the velocity models from the FWI and the tomography), and (c) the vertical velocity gradient (the derivative of velocity with respect to depth).

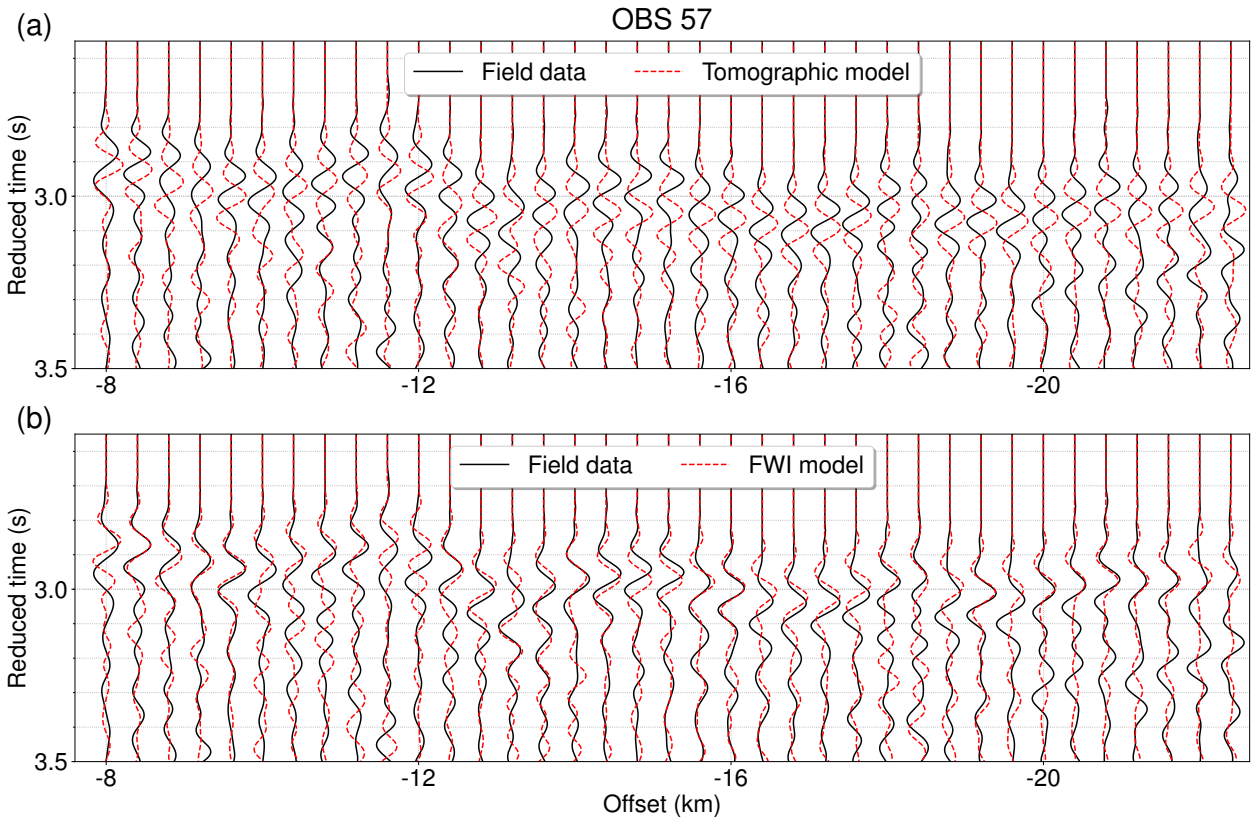

Fig. S4: Observed and synthetic seismic waveform data (trace-normalised) from OBS 57: (a) The recorded field data (black) and synthetic waveform (red) using the tomographic model (Extended Data Fig. 1), and (b) the recorded data (black) and synthetic waveform (red) using the trace-normalised FWI model (Extended Data Fig. 6). A reduced travel time of 7 km/s velocity was applied to both the field and synthetic data. Each trace in both the field and synthetic data has been normalised by the norm-2 of the trace itself.

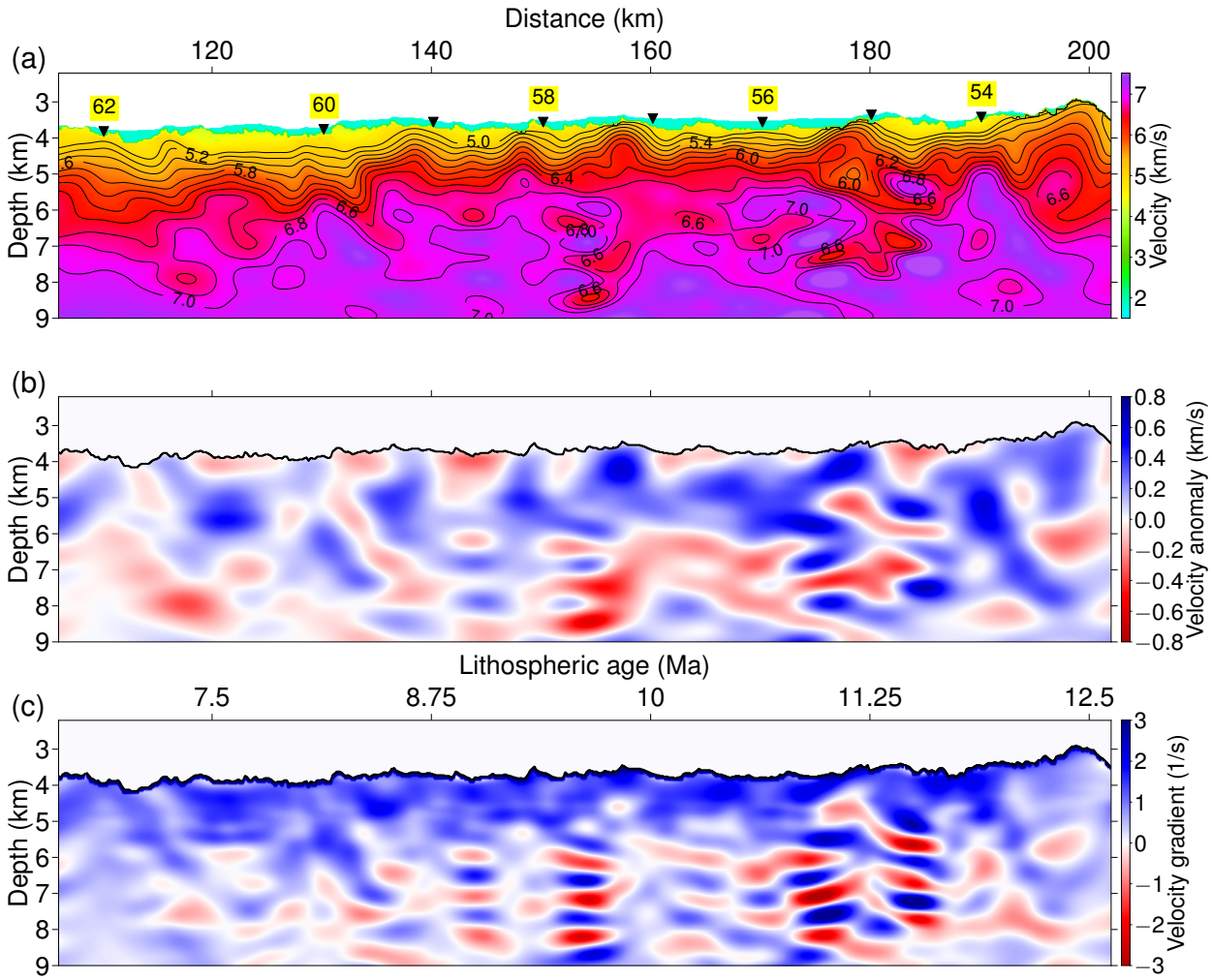

Fig. S5: Seismic velocity models of the oceanic crust from the 'true-amplitude' FWI without the intermediate trace-normalised FWI step. A Gaussian smoothing operator (smoothing length of 2 km and 0.4 km in the horizontal and vertical directions, respectively) was applied for velocity update. (a) The velocity model from the 'true-amplitude' FWI, (b) the velocity anomaly (the difference between the velocity models from the FWI and the tomography), and (c) the vertical velocity gradient (the derivative of velocity with respect to depth).

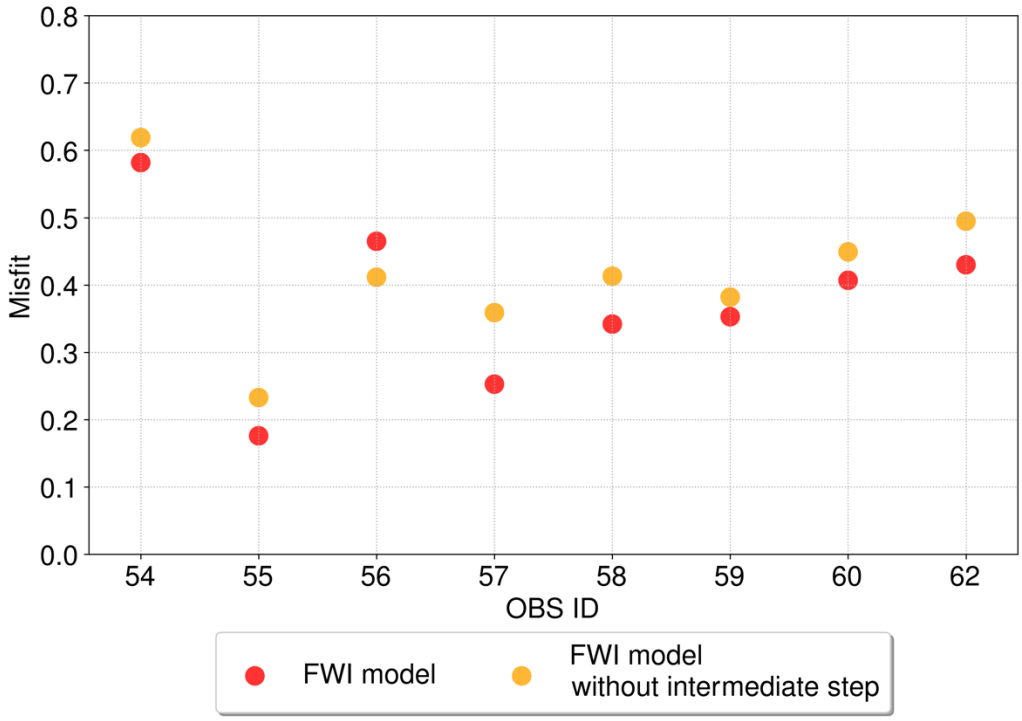

Fig. S6: Data misfit for each of the 8 OBS gathers from the true-amplitude FWI model in Fig. 2, and the true-amplitude FWI model in Fig. S5 without the intermediate step of trace-normalised FWI. The data misfit was calculated using Equation 2 in the Method section and then normalised to the same scale as in Extended Fig. 5.

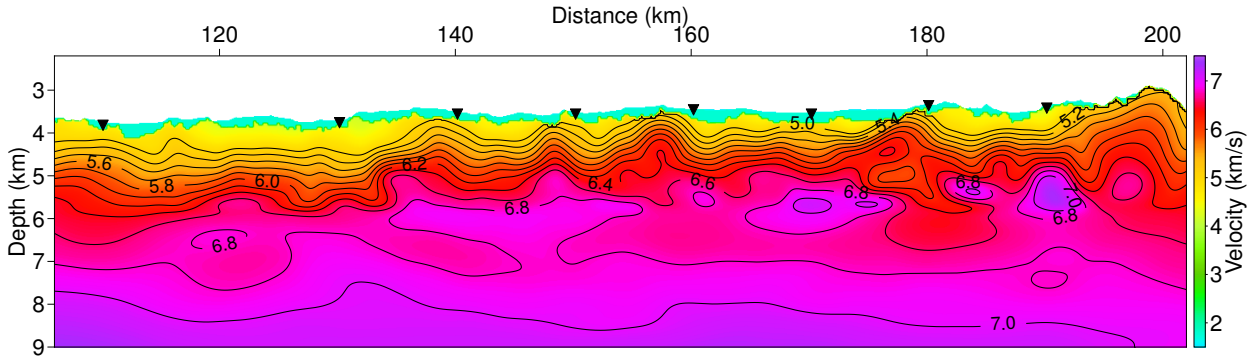

Fig. S7: Modified velocity model: The layered structures in the lower crust from 6 km depth in the velocity model from the FWI (Fig. 2) were removed and replaced by the corresponding trace-normalized FWI model at these depths (Extended Data Fig. 6) for synthetic modeling and inversion analysis. This altered model was used as a starting model for various FWI tests (Figs. S8-S13).

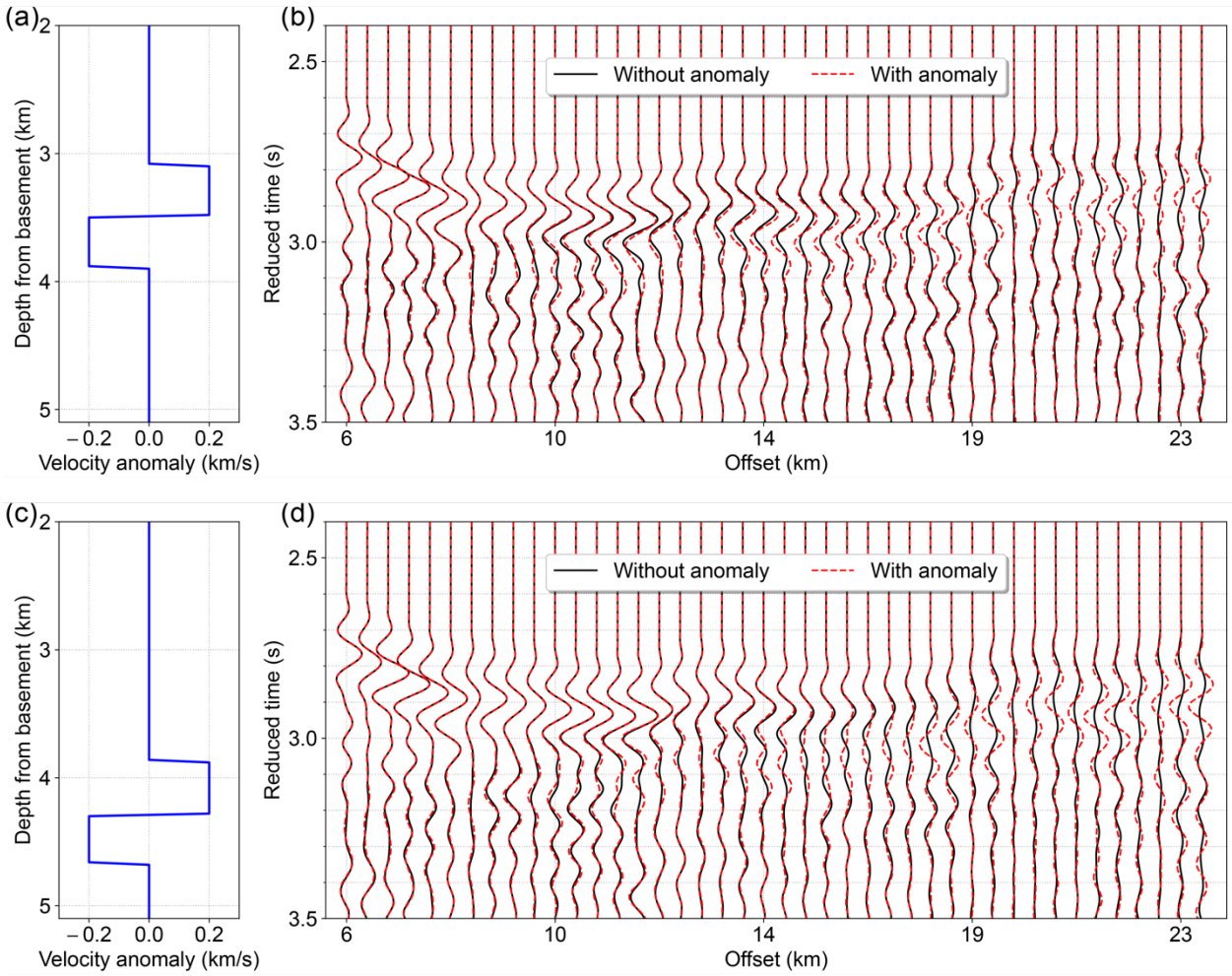

Fig. S8: Synthetic full waveform modeling tests: (a) and (c) shows the layered anomalies which were added to velocity model in Fig. S7 at the depth range of lower crust. (b) and (d) shows the simulated seismograms for velocity models with and without the layered anomalies.

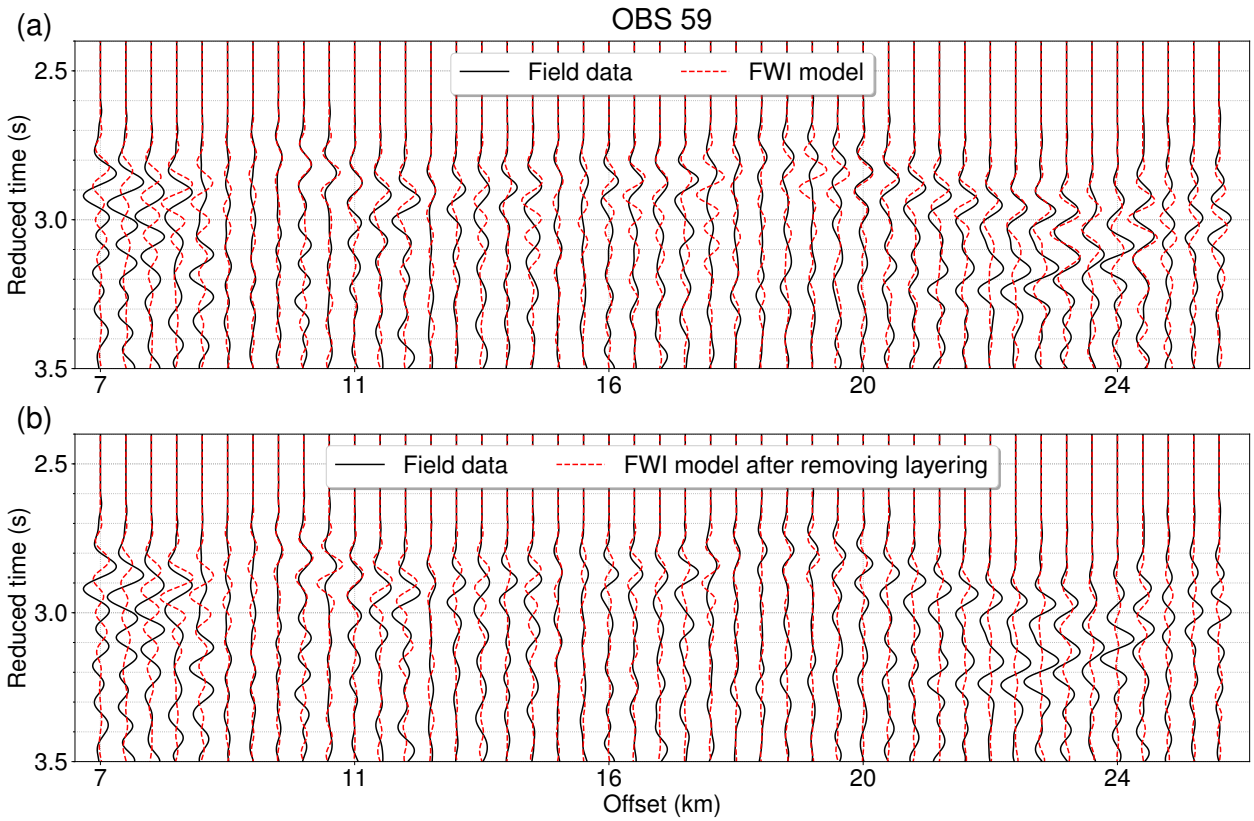

Fig. S9: Data comparison for OBS 59: (a) The recorded field data (black) and synthetic waveform (red) using the FWI model (Fig. 2a), and (b) the recorded data (black) and synthetic waveform (red) using the FWI model after removing layering in the lower crust (Fig. S7). A reduced travel time of 7 km/s velocity was applied to both the field and synthetic data. A scalar weighting factor (Offset/6) was multiplied for each trace to boost amplitude at large offsets for visualisation.

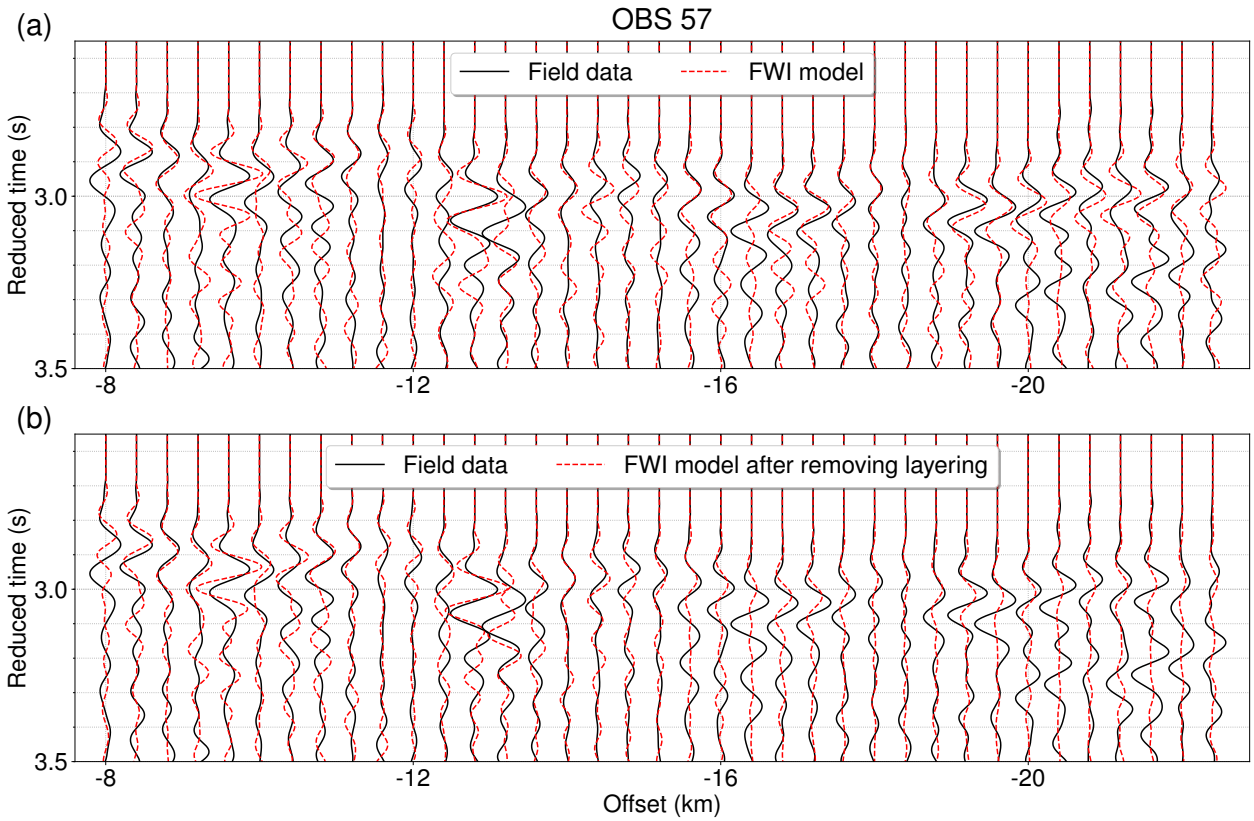

Fig. S10: Data comparison for OBS 57: (a) The recorded field data (black) and synthetic waveform (red) using the FWI model (Fig. 2a), and (b) the recorded data (black) and synthetic waveform (red) using the FWI model after removing layering in the lower crust (Fig. S7). A reduced travel time of 7 km/s velocity was applied to both the field and synthetic data. A scalar weighting factor (Offset/6) was multiplied for each trace to boost amplitude at large offsets for visualisation.

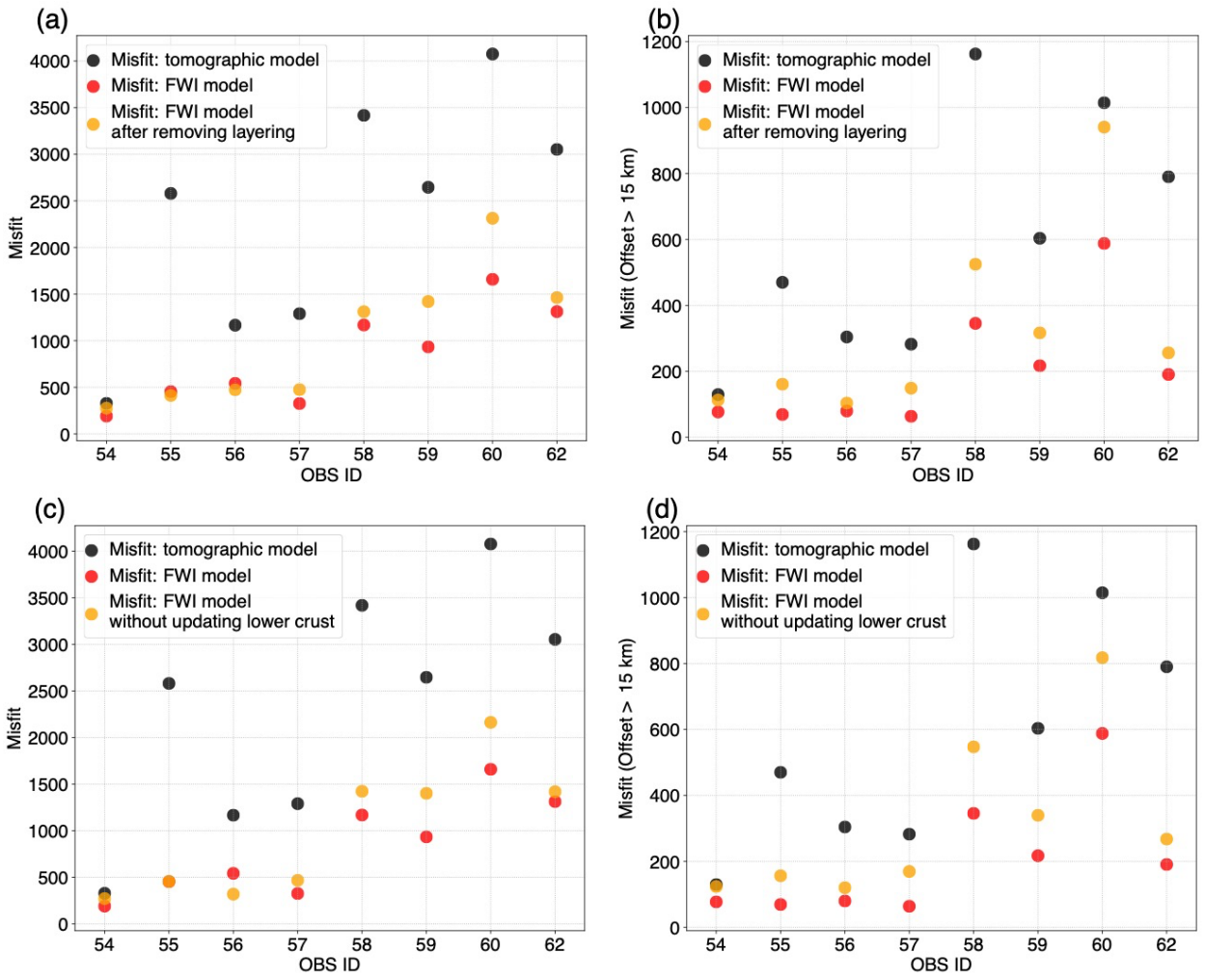

Fig. S11: (a) and (b) are data misfits for each of the 8 OBS gathers from the tomographic model (Extended Data Fig. 1), the FWI model after 80 iterations (Fig. 2), and the modified model (removing lower crustal layering, Fig. S7). (c) and (d) are data misfits for each of the 8 OBS gathers from the tomographic model (Extended Data Fig. 1), the FWI model after 80 iterations (Fig. 2), and the FWI test without updating the lower crust (Fig. S13). (a) and (c) show the misfits for full offsets, and (b) and (d) show the misfits for far offsets (larger than 15 km). The misfits are calculated using equation 2 in the Method section.

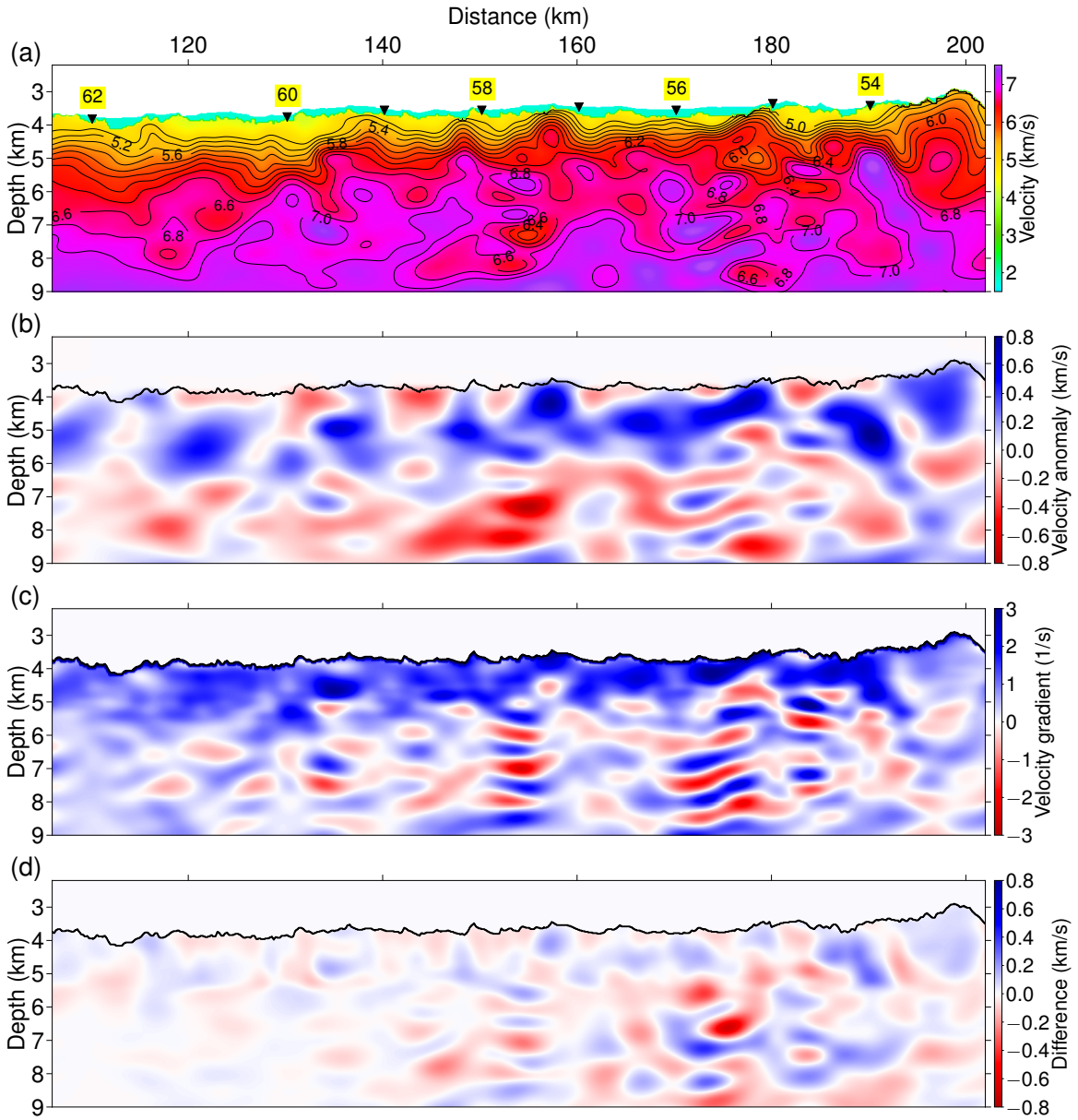

Fig. S12: Model recovery test: Seismic velocity models of the oceanic crust from the FWI using the altered model (Fig. S7) as the starting model. (a) The inverted velocity model from the FWI, (b) the velocity anomaly (the difference between the velocity model from the FWI and the tomography), (c) the vertical velocity gradient (the derivative of velocity with respect to depth), and (d) the difference between Fig. S12a and Fig. 2a. The recovered seismic models of the oceanic crust are very similar to those in Fig. 2.

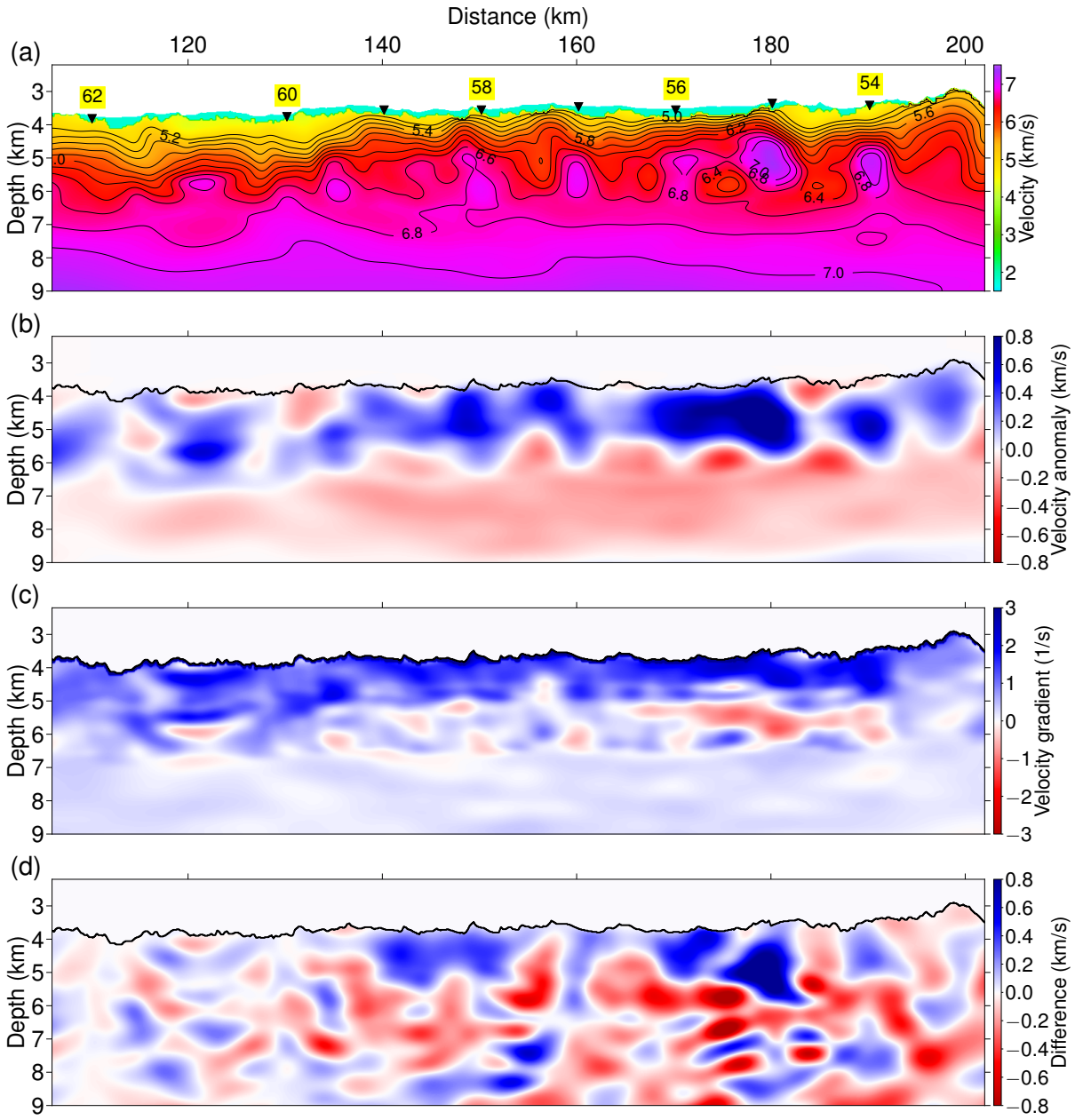

Fig. S13: Model recovery test: Lower part of the model greater than 2.5 km depth from basement is not updated during FWI. (a) The velocity model from the 'true-amplitude' FWI, (b) the velocity anomaly (the difference between the velocity models from the FWI and the tomography), (c) the vertical velocity gradient (the derivative of velocity with respect to depth), and (d) the difference between Fig. S13a and Fig. 2a.

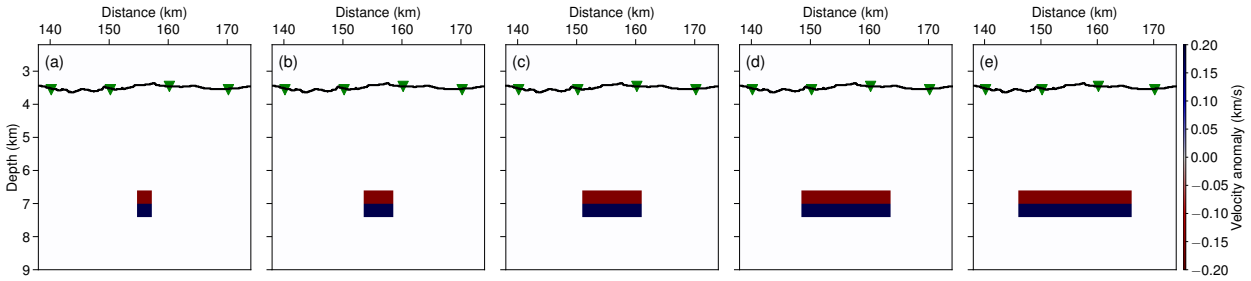

Fig. S14: Model perturbations for resolution study of Gaussian smoothing operators: here shows layering structures with - 200 m/s (upper layer) and + 200 m/s (lower layer) anomalies, with horizontal extension of (a) 2.5 km, (b) 5 km, (c) 10 km, (d) 15 km, and (e) 20 km, respectively. Thickness of each layer is 400 m. These model perturbations will be added to the tomographic model (Extended Data Fig. 1) for generating 'observed' data.

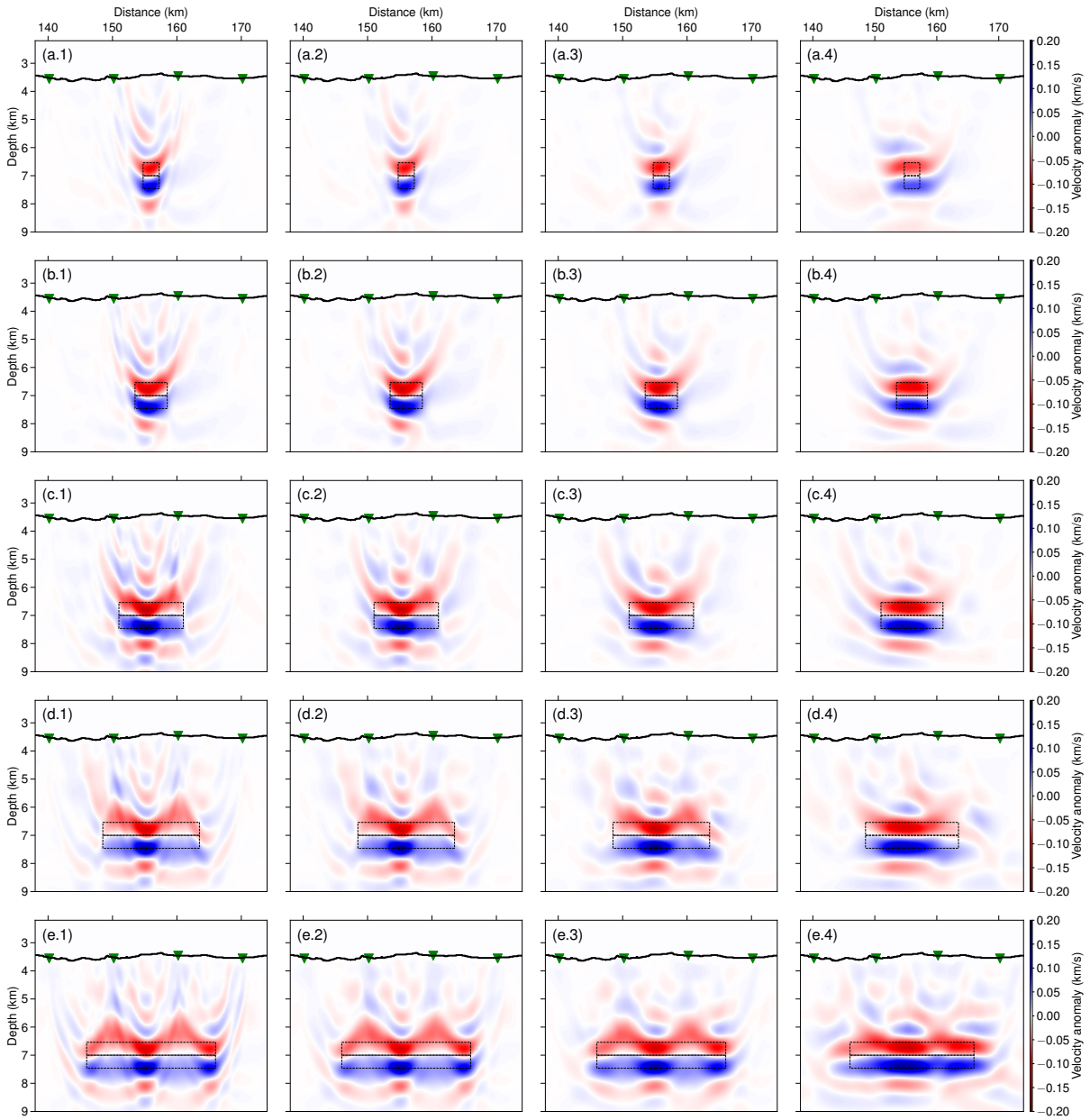

Fig. S15: Resolution study for different Gaussian smoothing operators: True model perturbations in Fig. S14 were added to the tomographic model (Extended Data Fig. 1) for generating the 'observed' data. FWI starts from the unperturbed tomographic model. From top to bottom, the layers have 2.5 km, 5 km, 10 km, 15 km, and 20 km lateral extensions, respectively. From left to right, the FWI-derived anomalies were obtained using horizontal smoothing lengths of 0.5 km, 1 km, 2 km, and 4 km, respectively. Smoothing length in the vertical direction is 0.4 km for all the tests. The shapes of the true anomalies were indicated by dashed lines.

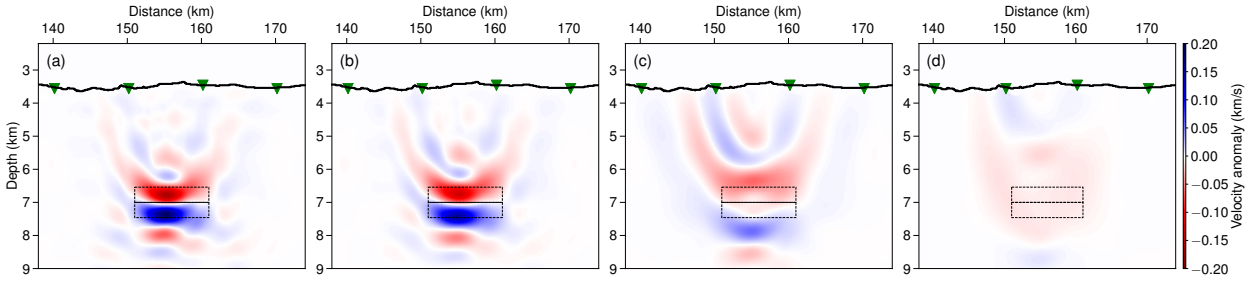

Fig. S16: Resolution study for different Gaussian smoothing operators: The velocity anomaly in Fig. S14(c) were added to the tomographic model (Extended Data Fig. 1) for generating the 'observed' data. Thickness of each layer is 400 m and horizontal extension is 10 km. FWI starts from the unperturbed tomographic model. From left to right, the FWI-derived anomalies were obtained using the smoothing lengths along the vertical direction of 0.2 km, 0.4 km, 0.8 km, and 1.6 km, respectively. Smoothing length in the horizontal direction is 2 km for all the tests. The shapes of the true anomalies were indicated by dashed lines.

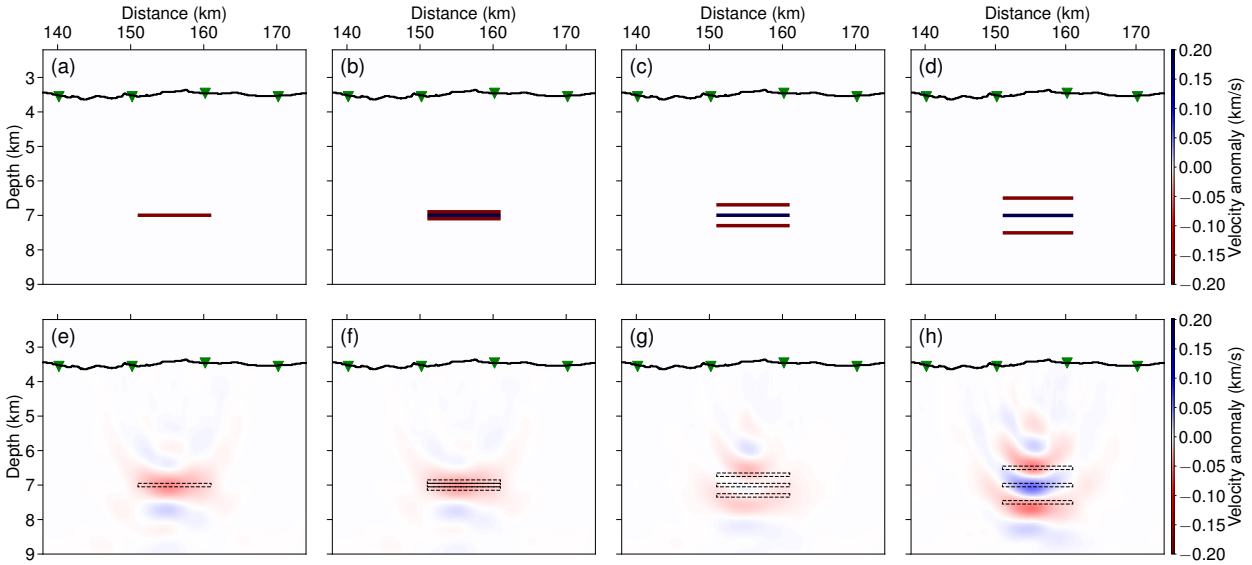

Fig. S17: Resolution study for thin layers with thickness of 100 m: (a) – (d) shows the true velocity anomalies which were added to the tomographic velocity model (Extended Data Fig. 1) for synthetic tests, respectively. (a) contains one layer of positive velocity anomaly, and (b)-(d) contain three layers with positive and negative anomalies. The vertical distances between layers in (c) and (d) are 200 m and 400 m, respectively. 'Observed' data was generated using the perturbed velocity model. FWI starts from the unperturbed tomographic model. A Gaussian smoothing operator (lengths of 2 km and 0.4 km in the horizontal and vertical directions, respectively) was applied for velocity update. (e) – (h) show the FWI-derived anomalies. The shapes of the true anomalies were indicated by dashed lines.

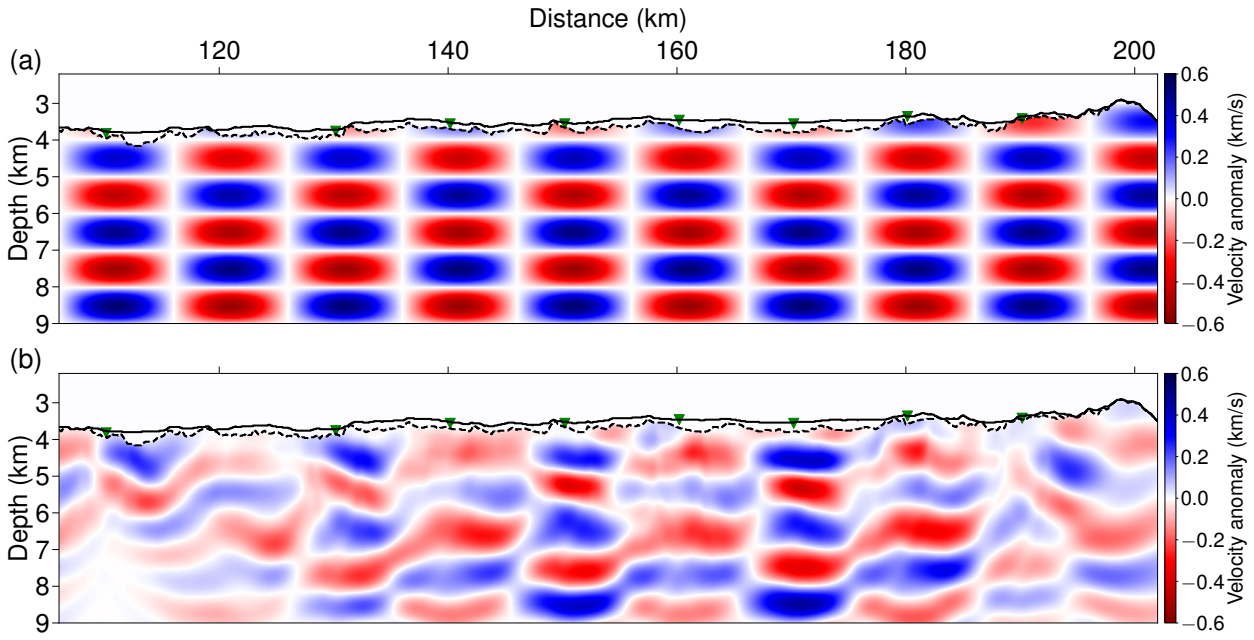

Fig. S18: Checkerboard test 1: The checkerboard model 1 was generated by adding 8% positive and negative Gaussian-shape velocity anomalies to the tomographic velocity model (Extended Data Fig. 1). Each of the anomalies has 10 km lateral extension and 1 km thickness. 'Observed' data was generated using the perturbed velocity model. FWI starts from the unperturbed tomographic model to see how well these perturbations can be recovered. (a) The true checkerboard velocity perturbation, and (b) the recovered velocity anomalies from the FWI. Note that the solid and dashed black lines at top indicate the bottom of the seawater and sedimentary layer (the top of layer 2), respectively.

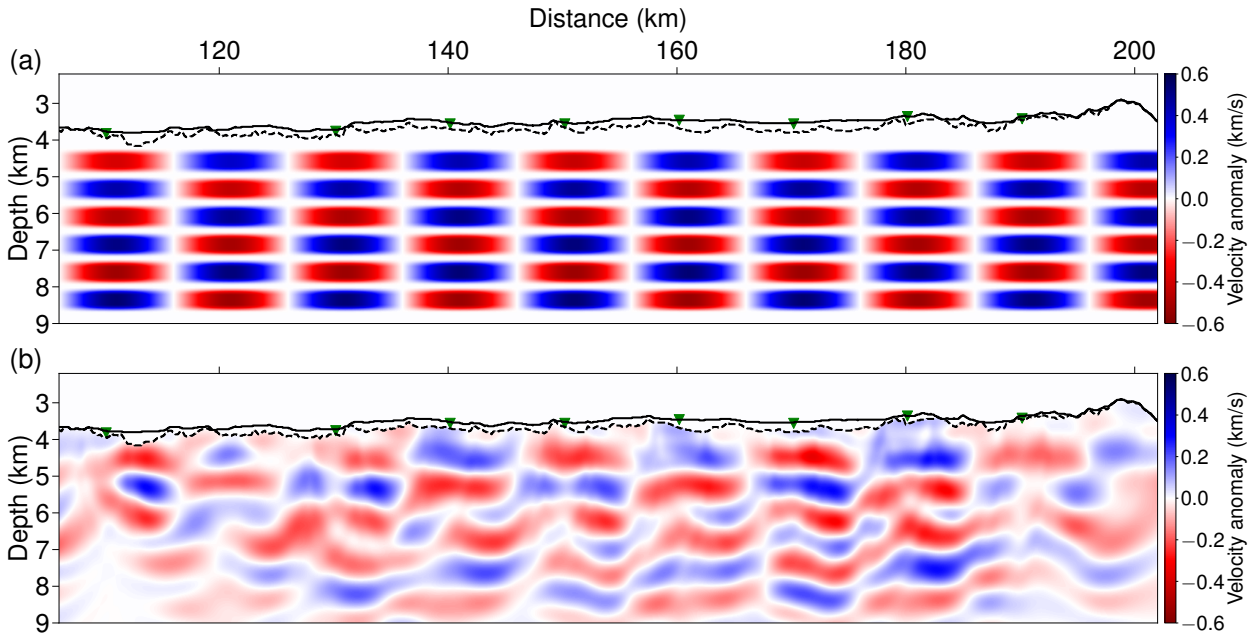

Fig. S19: Checkerboard test 2: The checkerboard model 2 was generated by adding 8% positive and negative Gaussian-shape velocity anomalies to the tomographic velocity model (Extended Data Fig. 1). Each of the anomalies has 10 km lateral extension and 0.5 km thickness. 'Observed' data was generated using the perturbed velocity model. FWI starts from the unperturbed tomographic model to see how well these perturbations can be recovered. (a) The true checkerboard velocity perturbation, and (b) the recovered velocity anomalies from the FWI. Note that the solid and dashed black lines at top indicate the bottom of the seawater and sedimentary layer (the top of layer 2), respectively.

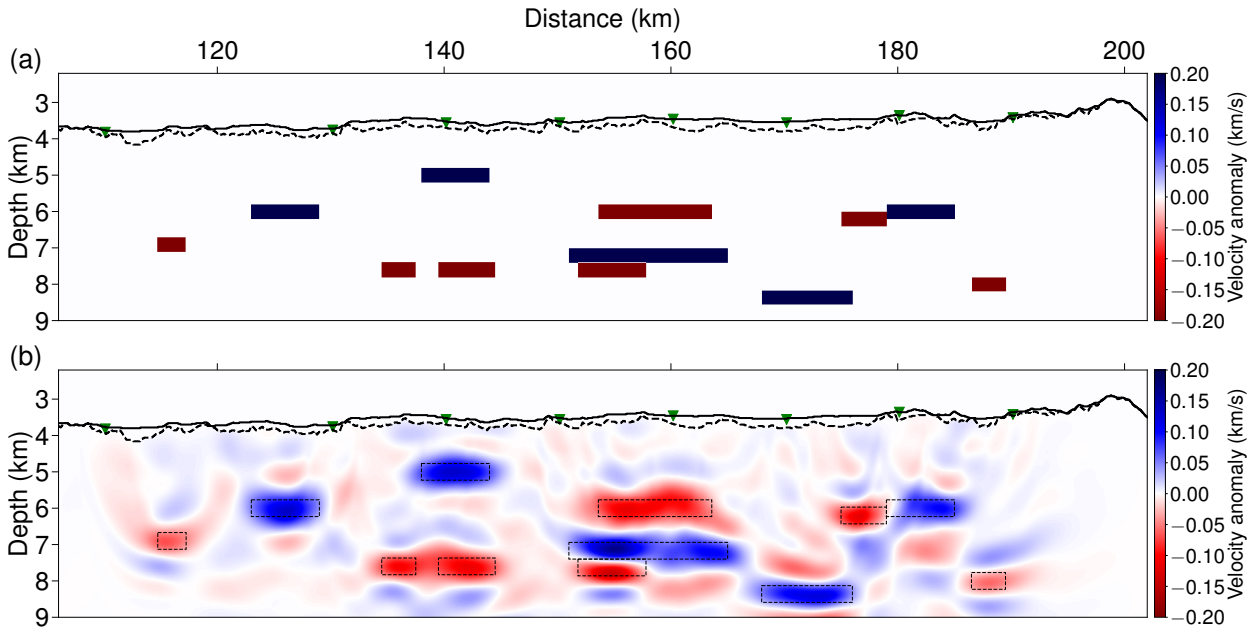

Fig. S20: Resolution study for random distributed anomalies: Random velocity anomalies of 0.4 km thickness and variable horizontal extensions and depths in (a) are added to the tomographic velocity model (Extended Data Fig. 1). 'Observed' data was generated using the perturbed velocity model. FWI starts from the unperturbed tomographic model to see how well these perturbations can be recovered. Note that the solid and dashed black lines at top indicate the bottom of the seawater and sedimentary layer (the top of layer 2), respectively.

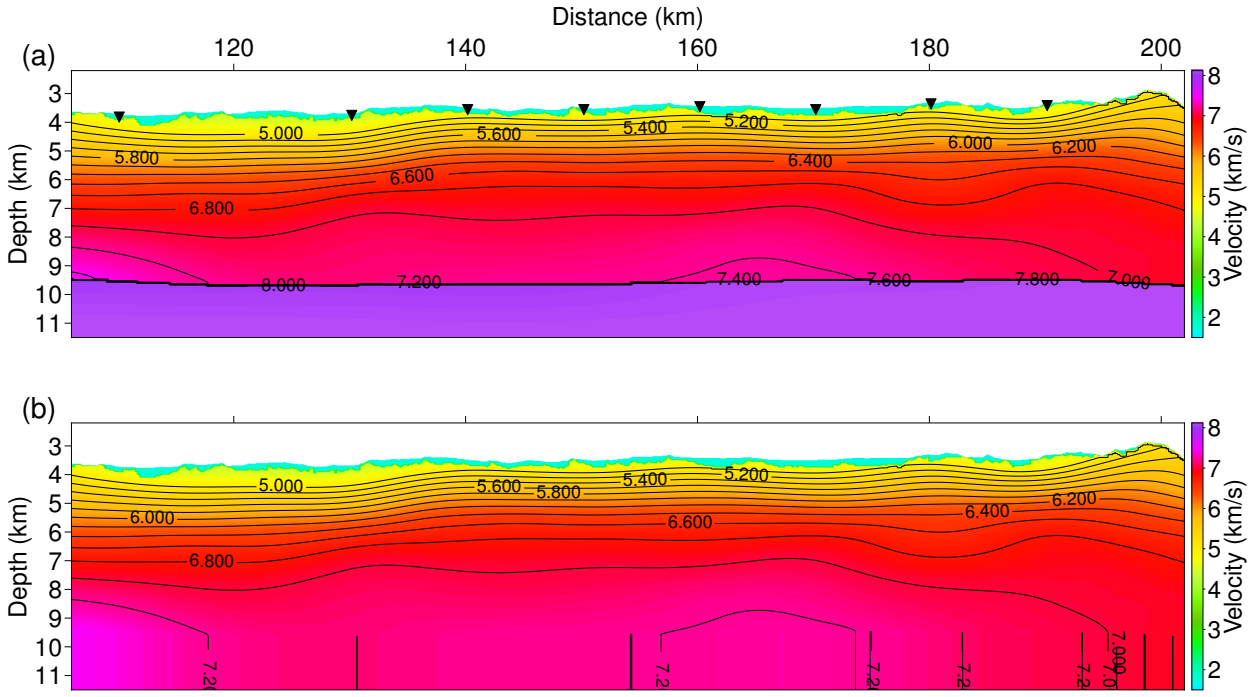

Fig. S21: Moho reflection interference test: (a) The velocity model[14] from travel-time tomography with Moho and upper mantle included was used as the 'true' model for generating 'observed' seismic data for FWI; (b) the same velocity model with (a) after removing the Moho and upper mantle (the velocities of these parts were replaced by velocities immediately above the Moho) was used as the starting velocity model for FWI.

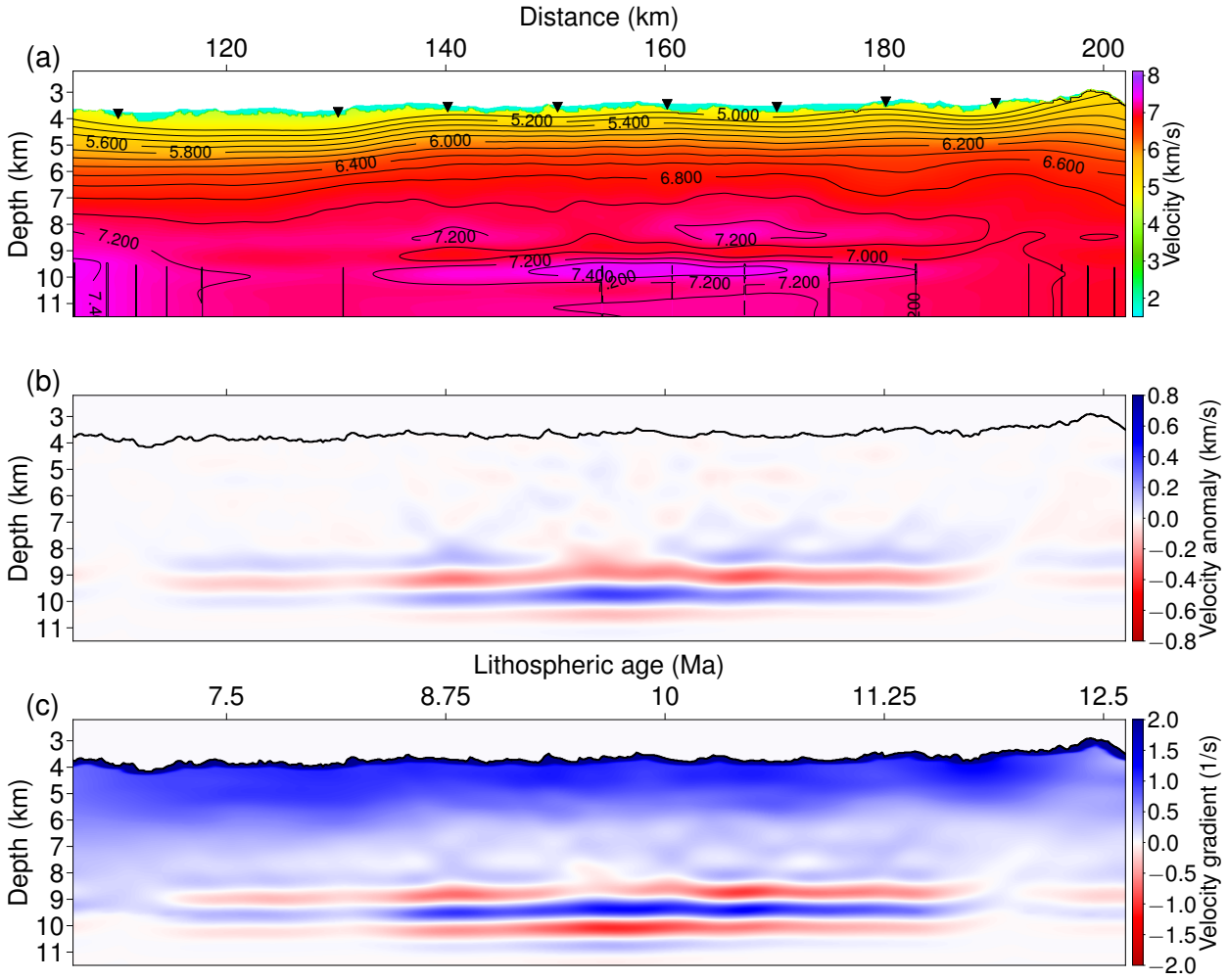

Fig. S22: Seismic images from FWI for the Moho interference test: (a) The velocity model from FWI, (b) the velocity anomaly (the difference between the velocity model from the FWI and the starting model), and (c) the vertical velocity gradient (the derivative of velocity with respect to depth). The velocity contours in (a) are from 5 to 7 km/s with an increment of 0.2 km/s. FWI was performed using the same source and receiver positions and frequency ranges of the data as in the actual observation, and the same inversion parameters. The same size window as for field data FWI, was used for including mainly Pg arrivals and reducing the influence of PmP at the far offsets from the 'observed' data for inversion.

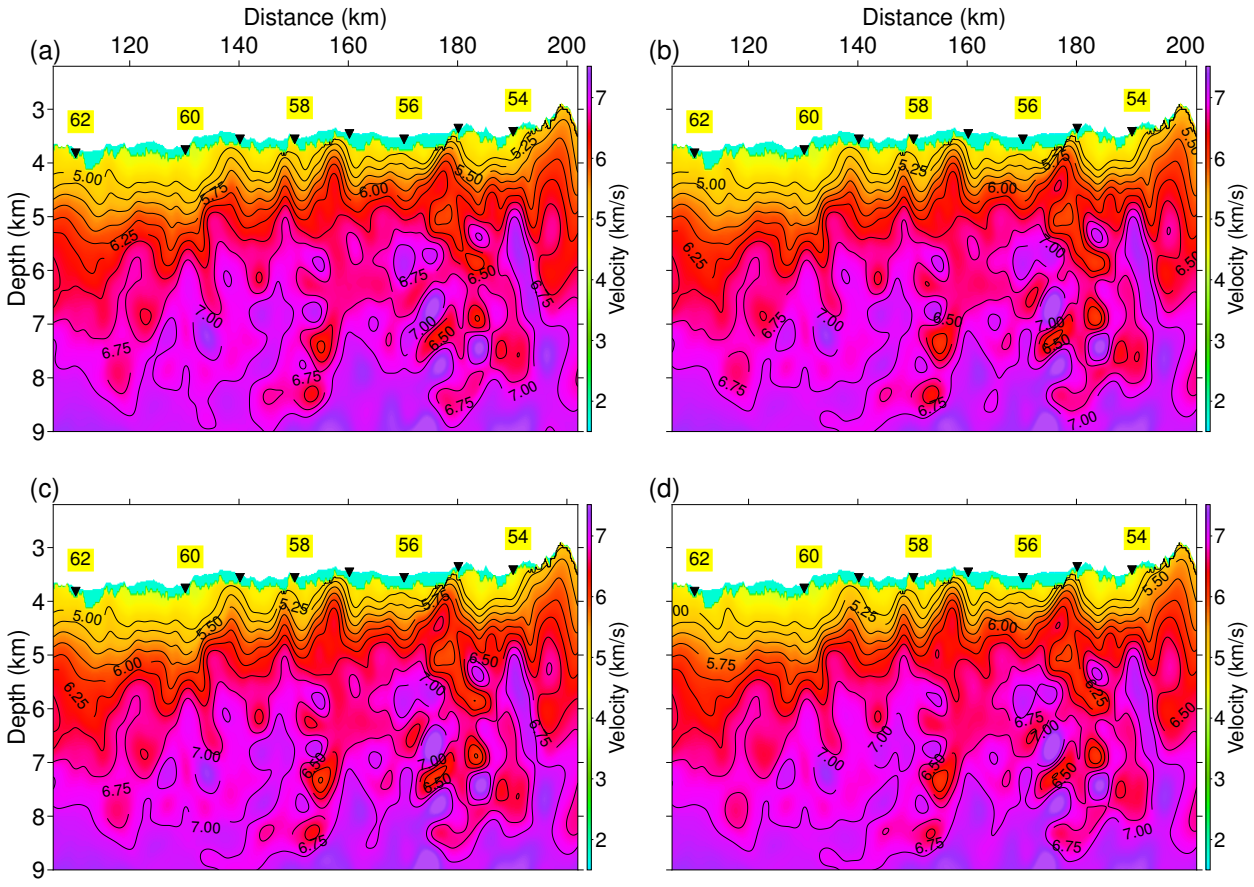

Fig. S23: Seismic velocity models from FWI for the size of muting time window: the muting time windows for (a) to (d) are 0.5 s (Fig. 2), 0.8 s, 1.2 s and 2.0 s, respectively. the velocity models are similar, except for some small differences mainly in the lower portion of the lower crust. We prefer a smaller time window for minimizing the influence of the PmP arrivals at far offsets (Figs. S1 and S2).

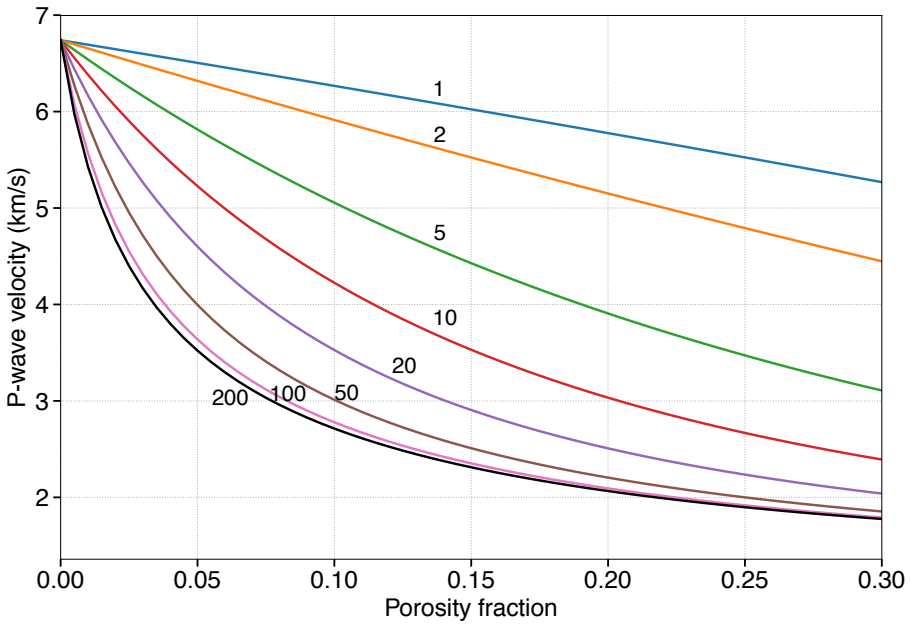

Fig. S24: P-wave velocity of basalt with increasing porosity. The differential effective medium model [Taylor and Singh, 2002] is used to calculate P-wave velocity for basalt with sea-water saturated cracks of increasing porosities. We consider different shapes (labelled in the figure, inverse of aspect ratios) of cracks. We set the P-velocity of basalt at zero porosity as 6.74 km/s and the density as 2930 kg/m^3. The S-velocity for basalt is obtained as 3.89 km/s using a Poisson's ratio of 0.25. The circulating sea-water saturating the porous basalt has P-wave velocity of 1.5 km/s, S-wave velocity of 0 km/s and 1030 kg/m^3 of density.

Taylor, M. A. J. & Singh, S. C. Composition and microstructure of magma bodies from effective medium theory. Geophys. J. Int. 149, 15–21 (2002).